Mapping Anisotropy and Triaxiality Effects in Magnesium Alloys

Padmeya P. Indurkar, Shahmeer Baweja, Robert Perez, Amol Vuppuluri, and Shailendra P. Joshi

Abstract

Microstructure, material properties, and macroscopic stress state closely interact in determining the strength and fracture resistance of ductile metals. While a fair understanding of the microstructure-stress interaction on strength, deformation stability, and damage has been achieved for common engineering alloys, the same is not true for magnesium (Mg) alloys. A fundamental understanding of how the net plastic anisotropy influences the macroscopic load-deformation characteristics and deformation stability will potentially aid the development of high-performance Mg alloys. A concerted multi-scale computational effort is essential in providing a deeper understanding of the deformation micromechanics of Mg alloys. In this paper, we investigate the microstructure-property linkages under tensile and compressive loading states through high-fidelity crystal plasticity modeling and simulation. Extended investigations along this path should enable the development of guidelines for damage-tolerant design of Mg alloys.

Keywords

HCP materials • Texture • Statistical response • Crystal plasticity • Plastic anisotropy

P. P. Indurkar
Department of Mechanical Engineering, National University of Singapore, Singapore, 117575, Singapore

P. P. Indurkar · S. Baweja · R. Perez · A. Vuppuluri · S. P. Joshi (✉)
Department of Mechanical Engineering, University of Houston, Houston, TX 77204-4006, USA
e-mail: shailendra@uh.edu

Introduction

Magnesium (Mg) alloys are promising candidates as lightweight structural metals owing to their high power-to-weight ratio. However, its low symmetry hexagonal close packed (HCP) crystal induces complex plastic behavior, which may have implications on the macroscopic properties such as ductility and formability. Although the HCP crystal structure hosts a large number of slip systems, it often suffers from the deficiency in the number of slip modes for general plastic straining by slip from the viewpoint of the von Mises criterion. This paucity of slip deformation is negotiated by the occurrence of deformation twinning. Moreover, the slip and twin modes vary significantly, both in their critical strengths and hardening behaviors, and exhibit complex interactions with each other resulting in intrinsic plastic anisotropy and tension-compression asymmetry at the single crystal scale. Notably, the anisotropic and asymmetric behaviors are pervasive even in polycrystals, particularly in highly textured microstructures.

Understanding the interaction between intrinsic and induced plastic anisotropy, texture, damage, and stress state are important to enable designing strong, fracture-resistant Mg alloys [1–8]. Recent work has focused on textural effects in the response of notched single crystal and polycrystalline specimens under tensile loading [3, 5]. Similar studies under compressive loading states are lacking.

In this work, we interrogate the role of plastic anisotropy —intrinsic and textural on the material response of Mg alloys. In particular, we simulate polycrystalline aggregate representative volume elements (RVEs) with synthetic textures that mimic experimental rolling textures and investigate their behaviors under tensile and compressive states. In doing so, the RVE explicitly resolves individual grains, and the plasticity within each grain is modeled using a three-dimensional crystal plasticity framework [9]. Our primary interest here is to understand the structure-property linkages of *damage-free* Mg alloys. To that end, we extract

the statistical aspects of yield and hardening behaviors, macroscopic deformation anisotropy, and textural evolution. The stochastic macroscopic behaviors are related to the relevant microscale deformation mechanisms. We analyze these behaviors for two levels of intrinsic (defined at the level of a single crystal) plastic anisotropy—one with a high anisotropy (representing pure Mg) and the other with a relatively lower intrinsic anisotropy (e.g. AZ31).

Model Formulation

Polycrystalline Aggregate FEM Model

Three-dimensional Voronoi tessellations of a cubic domain are generated using the Tessellation module ($-T$) in NEPER [10]. The cubic domain of dimension L_0 comprises N_g grains. Figure 1 shows the polycrystal representative volume element (RVE) with $N_g = 300$. The tessellation is kept fixed to mitigate any second-order effects arising from topological deviations. The RVE is meshed using meshing module ($-M$) in NEPER with nearly 84,000 fully integrated tetrahedral finite elements with each grain comprising about 279 finite elements. Such a fine finite element discretization is deemed sufficient based on our recent study [5]. The discretized RVE is exported to ABAQUS/STANDARD®, which embeds textural information described in the following paragraph.

Individual grains within the RVE are characterized by distinct crystallographic labels, which are essentially the sets of Euler angles (Fig. 1) $[E] = \left[\bar{\varphi}_1 \pm \varphi_1^\sigma, \bar{\Phi} \pm \Phi^\sigma, \bar{\varphi}_2 \pm \varphi_2^\sigma\right]$. Each Euler angle is assumed to follow a normal distribution with mean values $[\bar{\varphi}_1, \bar{\Phi}, \bar{\varphi}_2]$ and standard deviations $\varphi_1^\sigma, \Phi^\sigma, \varphi_2^\sigma$. Focusing on rolled sheet materials [1], the texture is assigned as follows: First, each grain g within the RVE is initialized as a single crystal with its principal crystal axes, $[1\bar{2}10], [10\bar{1}0]$ and $[0001]$, respectively, aligned with the sheet axes—rolling (L), transverse (T), and the short-transverse (S) directions. Next, setting $\bar{\varphi}_1 = \bar{\Phi} = \bar{\varphi}_2 = 0$, we randomly[1] pick three Euler angles $\left[E^g = \varphi_1^g, \Phi^g, \varphi_2^g\right]$ from their respective normal distributions that are bounded by $\pm 3\varphi_1^\sigma, \pm 3\Phi^\sigma, \pm 3\varphi_2^\sigma$ (Table 1). Next, a rotation matrix resulting from $[E^g]$ is applied to the initial aligned crystal axes to align it with respect to the sheet axes (L-T-S). A second rotation matrix is used to map the L-T-S triad with the global x–y–z triad (loading frame) such that the L-direction is aligned with the y-axis, which is the global loading direction. All the Euler angle sets $[E^g]$ are accounted for with this additional rotation to achieve the textured crystal geometry aligned along loading direction.

---

[1] We use the *randn* utility in MATLAB®.

A nominal strain rate $\left(\dot{\varepsilon}^{app} = 1 \times 10^{-3} s^{-1}\right)$ is applied along y-direction. To ensure a uniaxial stress state, $\dot{\varepsilon}^{app}$ is applied at the mid-node of the RVE top-face, while the bottom-face is restricted from translating along the y-direction thereby also arresting RVE rigid rotations about the x- and z-directions. Similarly, the left-face is restricted from translating along x-direction thereby also arresting rigid rotations about y-axis. Intersection node of front, left, and bottom faces is pinned to avoid translation along z. Hence, the RVE deforms longitudinally through top-face (along y-axis) and laterally through right and back faces (along the x- and z-directions, respectively). The macroscopic stress state generated in the RVE is $\Sigma = \Sigma_{yy}(e_y \otimes e_y)$, where e_y is the unit vector in the y-direction. The macroscopic logarithmic state of strain generated by this stress state is $\mathbf{E} = E_{xx}(e_x \otimes e_x) + E_{yy}(e_y \otimes e_y) + E_{zz}(e_z \otimes e_z)$ where $E_{xx} = \ln(L_x/L_0)$, $E_{yy} = \ln(L_y/L_0)$, and $E_{zz} = \ln(L_z/L_0)$. The Lankford ratio is calculated as $R_L = E_{TT}/E_{SS} = E_{xx}/E_{zz}$. Finally, the von Mises equivalent stress is $\Sigma_{eq} = \sqrt{(3/2)\Sigma':\Sigma'} = |\Sigma_{yy}|$, and the corresponding effective strain is $E_{eq} = \sqrt{(2/3)\mathbf{E}':\mathbf{E}'}$ where Σ' are the deviatoric stresses and $\mathbf{E}'$ are the corresponding deviatoric strains.

HCP Crystal Plasticity

The constitutive material considered here comprises 18 slip systems and 12 twin systems (Table 2), and a finite strain rate-dependent viscoplastic flow rule is employed for each of these plasticity modes using rate-tangent method, followed with twinning/spin-induced lattice reorientation. A detailed algorithmic description of this scheme and its FE implementation can be found in [9]. Two sets of material parameters are considered. In Table 3, one set of parameters is representative of 99.97% pure Mg; the corresponding set of parameters in the parentheses is representative of an Mg alloy (AZ31B) [3, 5].

Results and Discussion

Tensile Response

Figure 2a shows the stochastic responses of pure Mg and an Mg alloy (AZ31) under uniaxial tensile loading along the rolling direction (L). The solid lines with symbols denote the average response of the five textures (Table 1), and the shaded regions indicate one standard deviation resulting from textural deviations. Figure 2a indicates that, when loaded in tension along the L-direction, a reasonably large textural variation (case E is $\sim 30\%$ weaker than case A) does

Fig. 1 Definition of crystal orientations in a polycrystal aggregate of HCP single crystals. The sheet directions L, T, and S are, respectively, aligned with the global y, x, and z axes. Typical FE mesh details of a grain are shown
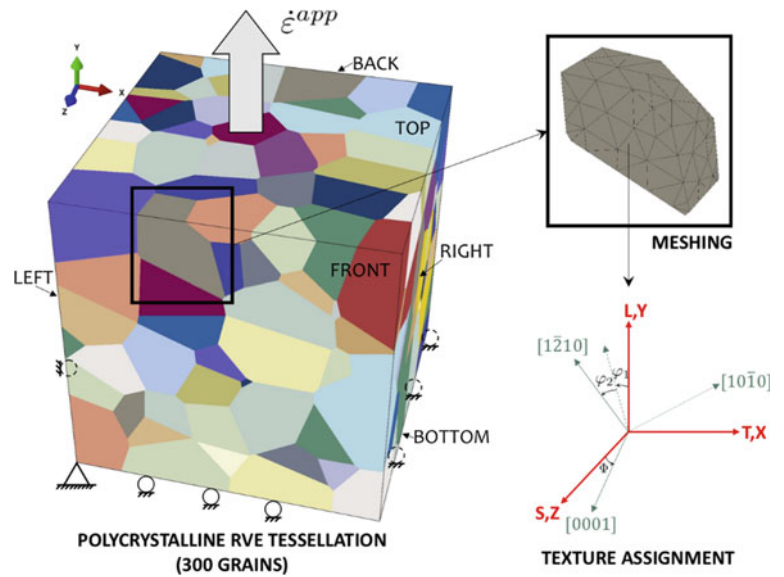

POLYCRYSTALLINE RVE TESSELLATION
(300 GRAINS)

TEXTURE ASSIGNMENT

Table 1 Texture cases considered in this work

Angles↓/cases→	A (°)	B (°)	C (°)	D (°)	E (°)
φ_1^σ	20	20	30	30	30
Φ^σ	10	20	10	20	20
φ_2^σ	0	0	0	0	10

Table 2 Slip and twin systems observed in Mg single crystals

Mechanisms	Slip/twin plane	Slip/twin direction	No. of systems
Basal $\langle a \rangle$ slip	(0001)	$\langle 11\bar{2}0 \rangle$	3
Prismatic $\langle a \rangle$ slip	$\{10\bar{1}0\}$	$\langle 11\bar{2}0 \rangle$	3
Pyramidal $\langle a \rangle$ slip	$\{10\bar{1}1\}$	$\langle 11\bar{2}0 \rangle$	6
Pyramidal $\langle c+a \rangle$ slip	$\{11\bar{2}2\}$	$\langle 11\bar{2}3 \rangle$	6
Extension twinning	$\{10\bar{1}2\}$	$\langle 10\bar{1}1 \rangle$	6
Contraction twinning	$\{10\bar{1}1\}$	$\langle 10\bar{1}\bar{2} \rangle$	6

Table 3 Material properties for pure Mg and (in brackets) Mg alloy (AZ31B)

Mechanisms	τ_0(MPa)	h_0(MPa)	τ_s(MPa)		$\tau_0^i/\tau_0^{\text{pris.asl.}}$
Basal $\langle a \rangle$ slip	0.5 (10)	20 (50)	–		0.02 (0.18)
Prismatic $\langle a \rangle$ slip	25 (55)	1500	85 (110)		1
Pyramidal $\langle a \rangle$ slip	25 (55)	1500	85 (110)		1
Pyramidal $\langle c+a \rangle$ slip	40 (60)	3000	150 (170)		1.6 (1.09)
Extension twinning	τ_0(MPa)	h_{et}(MPa)	$\tau_{\text{s\_et}}$(MPa)	$h_{\text{et\_sl}}$(MPa)	0.14 (0.27)
	3.5 (15)	100 (120)	20 (30)	100	
Contraction twinning	τ_0(MPa)	H_{ct}(MPa)	$H_{\text{ct\_sl}}$(MPa)	b	2.2(1.55)
	55 (85)	6000	15	0.05	

not result in a significant variation in the overall stress–strain response. Further, the standard deviation about the mean tends to decrease with increasing strain. Only over a narrow intermediate strain regime ($0.03 \leq E_{\text{eq}} \leq 0.06$) does the deviation appear to be of some significance. The upper bound of the standard deviation coincides with case A, while the lower bound coincides with case E. Moreover, these observations hold in both cases, which suggest that the

Fig. 2 Stress–strain $(\Sigma_{eq} - E_{eq})$ responses and Lankford ratio (R_L^T) evolution under uniaxial tension along the rolling (L) direction

(a) Stress, L, Uniaxial Tension   **(b)** Lankford Ratio, L, Uniaxial Tension
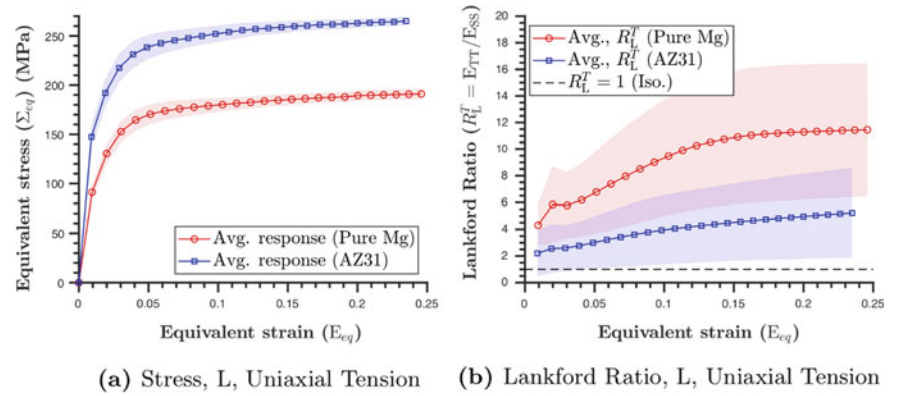
intrinsic crystallographic anisotropy plays a negligible role, if any, in the stochastic response of these materials.

In terms of the correlation between the yield strength and texture, $A > C > B > D > E$; the average response (solid lines with symbols) lies between cases C and B (for both pure Mg and Mg alloy), which indicates the stronger effect of variation of Φ than φ_1. It follows from the notion that deviations of $[1\bar{2}10]$ due to φ_1 variation do not cause a significant variability in yield strength as Mg is expected to exhibit transverse isotropy in the L-T plane. The higher strength and somewhat higher hardening in the Mg alloy relative to pure Mg are a consequence of the higher τ_0 and τ_s for the prismatic $\langle a \rangle$ mode—a favorable mechanism in both materials (cf. Fig. 3b).

In comparison, the lateral deformation anisotropy defined by the Lankford ratio $R_L^T = E_{TT}/E_{SS}$ is more sensitive to textural deviations (Fig. 2b). For a given material, it deviates significantly from isotropy ($R_L^T = 1$). Pure Mg exhibits an overall higher lateral anisotropy compared to the Mg alloy. The average value of R_L^T for pure Mg is ~ 8 while that for the Mg alloy is ~ 3. These values are consistent with recent studies on smooth and notched rounded bars [1, 5]. The effect of texture and material anisotropy on R_L^T for smooth cylindrical tensile specimens was discussed in [3, 5] which concluded in lateral anisotropy causing elliptical cross sectioned specimens with the S- and T-directions as the major and minor axes, respectively. Textured pure Mg specimens at areal notch strain of 0.2 had $R_L^T \sim 45$ for a textural variation defined by $[E^\sigma] = [30°, 0, 0]$. For a similar texture, the polycrystalline Mg alloy gave $R_L^T \sim 35$ while $R_L^T \sim 2.5$ for $[E^\sigma] = [0°, 10°, 0]$. The tempering of the lateral anisotropy in the Mg alloy seems to be related to the lower difference in the initial and saturation strengths of pyramidal $\langle a \rangle$ and pyramidal $c + a$ modes compared to pure Mg. In other words, the harder the pyramidal $\langle c + a \rangle$ the more difficult is the contraction of the c axis, which is on average oriented along S. Further, the evolution of Lankford ratio for pure Mg is more sensitive to the texture compared to Mg alloy.

Among the different textures, case C (case A is a close second) is most laterally anisotropic for both pure Mg and AZ31. On the other hand, in both materials, case D has the lowest R_L^T (and not case E as one would expect). That is, for a given φ_1, the lateral deformation anisotropy decreases with increasing Φ; on the other hand, if both φ_1 and Φ are held constant in the initial texture, a variation of φ_2 does not seem to push $R_L^T \to 1$. Instead, the deformation tends to become more anisotropic. Hence, case D consistently has a lower R_L^T (closer to 1) than case E for both materials.

Compressive Response

Figure 4a shows the average macroscopic response of the RVEs when loaded in compression along the rolling (L) direction. As in the tensile loading case, the shaded regions indicate one standard deviation resulting from textural variations (cf. Table 1). From the nature of the stress–strain responses, it is evident that extension twinning is a preferred and dominant deformation mode in the initial stages, which results in the characteristic sigmoidal response. Surprisingly, the effect of textural variation is even weaker than in the tensile loading case. Note that the anisotropy ratio of the CRSS values between extension twinning and pyramidal $\langle c + a \rangle$ is ~ 4 for the Mg alloy, while it is much larger (~ 11) for pure Mg. In other words, even with nearly 30% textural weakening (relative to the strong texture, case A) and $\sim 60\%$ enhancement of the CRSS for extension twinning, deformation twinning remains a dominant deformation mode, thereby producing an overall softer response under uniaxial compression along the L-direction.

In both material systems, the upper bound of the shaded regions corresponds to case C (case A is a close second), while lower bound corresponds to case B (case D is close). From the viewpoint of textures, deviations in Φ tend to weaken the post-twinning hardening. The intermediate hardening (between the two plateau-like regions) also depends on the textural strength, albeit weakly.

(a) $\bar{\zeta}^{\text{bas.}\langle a\rangle\text{sl.}}$

(b) $\bar{\zeta}^{\text{pris.}\langle a\rangle\text{sl.}}$

(c) $\bar{\zeta}^{\text{pyr.}\langle a\rangle\text{sl.}}$

(d) $\bar{\zeta}^{\text{pyr.}\langle c+a\rangle\text{sl.}}$

(e) $\bar{\zeta}^{ET}$ and $\bar{f}^{ET}$

(f) $\bar{\zeta}^{CT}$ and $\bar{f}^{CT}$
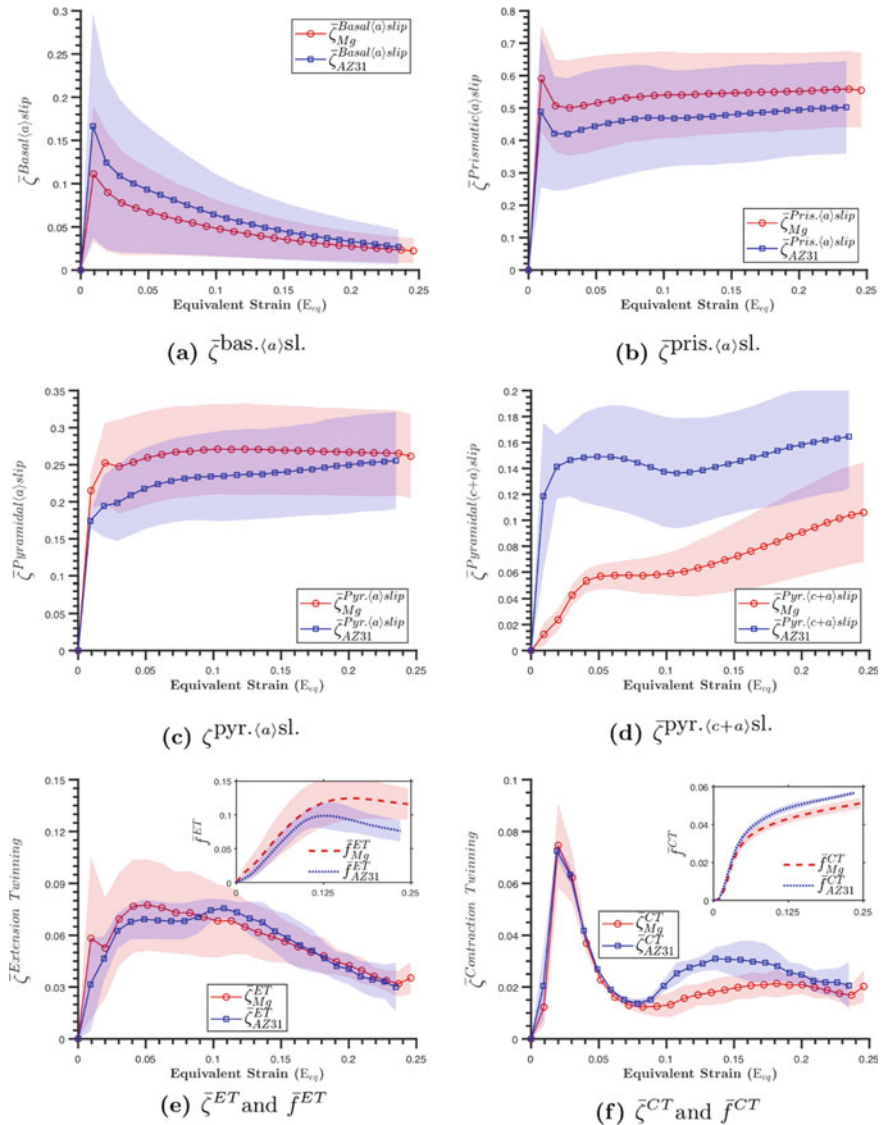
(a) Stress, L, Uniaxial Compression

(b) Lankford Ratio, L, Uniaxial Compression
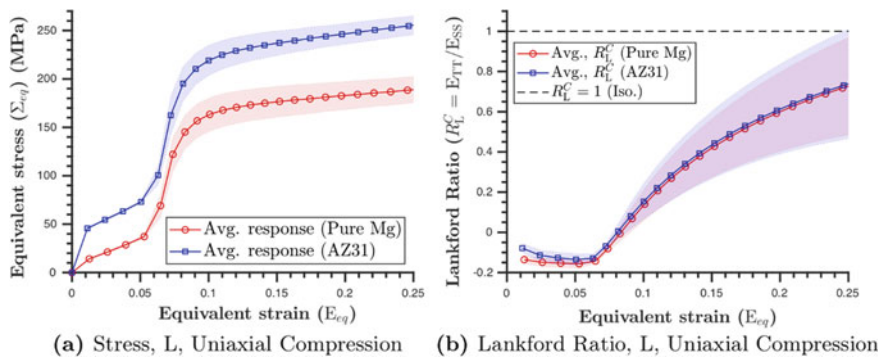
Interestingly, the evolution of Lankford ratios for both materials stands in stark contrast to its counterpart under the tensile loading on several counts (cf. Figure 4b). First, the qualitative nature of the evolution is different: it transitions from $R_L^C < 0$ to $R_L^T > 0$, unlike the tensile case where $R_L^T \gg 1$ throughout the deformation. The transition coincides with the equivalent strain at which the twinning-induced rapid hardening kicks in. Second, the ratio tends toward 1, indicating a decrease in the lateral strain anisotropy with progressive deformation. Physically, under uniaxial compression along the L-direction, the lateral extension along the S-direction is easier compared to that along the T-direction; in fact, extension along

the T-direction stagnates while that along the S-direction evolves rapidly during twinning. Due to textural variations, the $\langle c \rangle$ tends to be distributed in the L-T plane after the global reorientation process is largely complete, which results in a decrease in the rate of extension along the S-direction; at this stage, there is an increase in the extensional rate along the T-direction, which leads to $R_L^C \to 1$.

As in the tensile loading case, the variability in the Lankford ratios (in both materials) is much larger compared to the variability in the stress–strain response. However, unlike the tensile counterpart, their evolution, in an average sense, is insensitive to the intrinsic crystallographic anisotropy. Further, the Mg alloy appears to be more sensitive to textural variations than pure Mg, which is in contrast to the tensile loading scenario.

As seen from Fig. 5e, in the initial stages, extension twinning is indeed the primary carrier of plastic deformation accounting for $\sim 70 \pm 10\%$ of the deformation activity. In this regime, basal slip is the next dominant mode ($\sim 28 \pm 10\%$). Weaker initial textures promote $\bar{\zeta}^{\text{bas.}\langle a \rangle}$ (Fig. 5a), which can be understood by the fact that any variation of $\langle c \rangle$-axis on LS or TS planes (promoted by Φ) will increase the resolved stress on basal planes to the extent that a grain with LS axis oriented along the y-direction (i.e. $45°$ deviation), will result in the maximum Schmid factor on the basal planes. Given that the τ_0 and hardening rates (h_0 and h_{et}) for both these mechanisms are much lower than other deformation modes, they dominate the overall plasticity in the initial regime prior to twinning-induced reorientation. Accumulated f_{et} before reorientation is $\sim 70\%$ for

Fig. 5 Average relative activities of different mechanisms ($\bar{\zeta}^i$) and twinning volume fraction (f^i) evolution responses for the polycrystalline textures considered under uniaxial compression along the rolling (L) direction

both materials reinforcing the pervasive nature of twinning even in weaker textures. After reorientation, pyramidal $\langle c+a \rangle$ dominates the response for both materials accounting for $\sim 70 \pm 5\%$ of the total deformation activity; the remainder contributions come from prismatic $\langle a \rangle$ and pyramidal $\langle a \rangle$ modes. Interestingly, unlike in the tensile loading case where pure Mg showed much higher pyramidal $\langle c+a \rangle$ activity compared to that in the Mg alloy, in the compressive loading case, it is largely insensitive to the intrinsic crystallographic anisotropy. Clearly, the large variability in the relative activities translates into the corresponding variability in the Lankford ratios (cf. Fig. 4b) that does not result in very high standard deviation in strength response as these mechanisms have similar CRSS and hardening responses.

Texture Evolution

Figure 6 is a collage of textural evolution under both loading states for the sharpest (case *A*), weakest (case *E*), and intermediate (case *D*) initial textures. The texture plots are created using MTEX [11]. Due to the variability of φ_1, the [$1\bar{2}10$] directions of individual grains deviate from the tensile loading direction (L). At the grain scale, with increasing φ_1, one of the two active prismatic $\langle a \rangle$ variants becomes a preferred system (based on a Schmid factor); as a result, lattice spin occurs causing crystal rotation that effects textural sharpening by pushing ($10\bar{1}0$) away from the initial pole along T towards L (cf. Fig. 6a, d). A further effect is that the intensity of ($10\bar{1}0$) poles along T is reduced. The relative reduction in the [0001] pole intensity is much smaller due to the dearth of the activity of mechanisms that can cause spin of $\langle c \rangle$ axis, namely pyramidal $\langle c+a \rangle$, ET, and CT (all <10%). Moreover, similar plastic strain accrual on the conjugate variants of these mechanisms will reduce the net spin.

Under compression, twinning causes an instantaneous change in texture. Apart from the significant shifting in the poles, the textural deviation is also marked by reduction in intensity of the newly aligned poles. Schmid analysis indicates that compression along the L-direction can activate
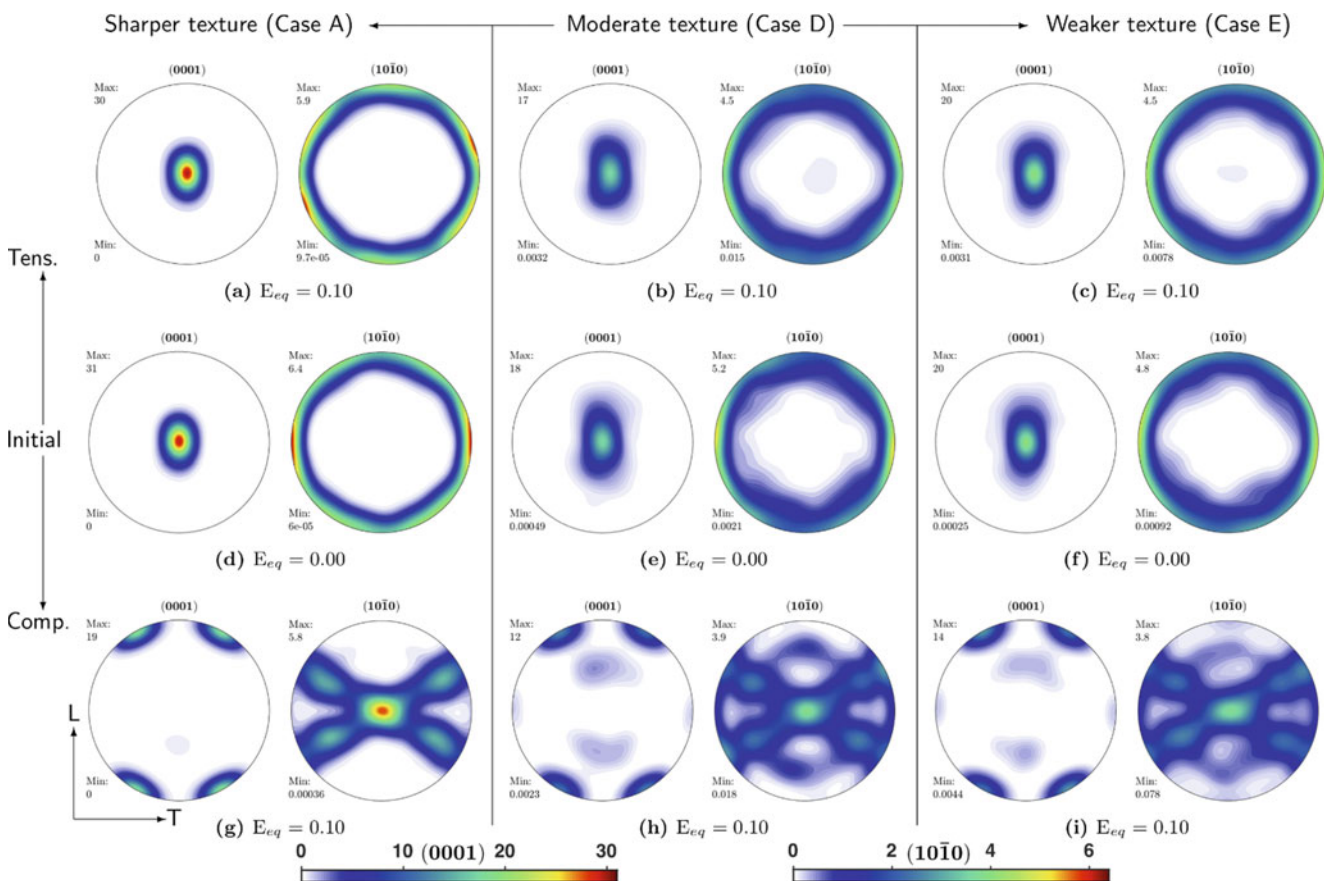

Fig. 6 Evolution of [0001] and [$10\bar{1}0$] pole figures on the LT plane for textures *A*, *D*, and *E* under uniaxial tension and compression along the rolling (L) direction. The central row shows initial textures, with central column being for moderate initial texture (case *D*), left for sharper initial texture (case *A*), and right for weaker initial texture (case *E*). Top row shows deformed texture under tension, while the bottom row shows deformed texture under compression (both at $E_{eq} = 0.10$). The color bars show intensities plotted in pole figures for [0001] (left) and [$10\bar{1}0$] (right) poles, respectively

four twin variants: $(0\bar{1}12)[01\bar{1}1]$, $(01\bar{1}2)[0\bar{1}11]$, $(1\bar{1}02)[\bar{1}101]$ and $(\bar{1}102)[1\bar{1}01]$; as such, an individual grain in the ensemble has equal probability of reorienting its $\langle c \rangle$ axis along one of these directions in the LT plane, effectively splitting the intensity of [0001] poles into these four regions. This transition is more evident for a sharper texture, cf. Figure 6d, g. The change in [0001] poles is correspondingly marked by the emergence of $[10\bar{1}0]$ poles out of the LT plane as shown in Fig. 6g.

An initial sharper texture undergoes relatively larger weakening with deformation (see maximum pole intensity values). For progressively weaker initial textures, the evolution remains qualitatively similar to the sharper texture, although with some additional aspects. In particular, note the emergence of two [0001] poles closer to the initial $[10\bar{1}0]$ poles on the LT plane. These poles are formed because, with increasing spread in texture, there is a decreasing resolved stress on the four twin variants most active in case A but marked by an increase in resolved shear stress on the remaining two variants $((10\bar{1}2)[\bar{1}011]$ and $(\bar{1}012)[10\bar{1}1])$ whose twin directions $([\bar{1}011]$ and $[10\bar{1}1]$, respectively) result in reoriented $\langle c \rangle$ axis along $\langle 10\bar{1}0 \rangle$. This also results in these reoriented grains having their $[10\bar{1}0]$ poles emerging on LT plane.

Summary: In this work, we investigate the stochastic behavior of Mg polycrystals by considering several synthetic textures that mimic experimental rolled textures. Focus is laid on quantifying the behavior under monotonic tensile and compressive loading along the rolling direction. The salient outcomes are as follows:

1. In tensile loading, the Lankford ratio increases with deformation, exhibiting a strong sensitivity to plastic anisotropy both, crystallographic and textural. This sensitivity is consistent with the sensitivity of the deformation mechanisms to textural variability. Yet, the variability of the deformation mechanisms (and by extension, of the lateral strains) does not reflect in the variability of the stress–strain responses. Interestingly, this observation holds even in the case of a high crystallographic anisotropy, e.g. pure Mg.
2. In compressive loading, even for relatively weak textures, the extension twinning mode governs the initial response. The stress–strain response is relatively insensitive to the initial texture during the stage, while extension twinning is active. However, the sensitivity of the stress–strain response to textural variability is exacerbated once twinning-induced material hardening occurs. In contrast to the tensile case, the Lankford ratio evolution is non-monotonic; the lateral strains approach

isotropic state at high strains. Moreover, the deformation anisotropy is insensitive to the intrinsic crystallographic anisotropy, unlike the tensile case.

References

1. B. Kondori and A. A. Benzerga, "Effect of Stress Triaxiality on the Flow and Fracture of Mg Alloy AZ31," *Metallurgical and Materials Transactions A,* vol. 45, no. 8, pp. 3292–3307, 2014.
2. B. Kondori and A. A. Benzerga, "On the notch ductility of a magnesium-rare earth alloy," *Materials Science and Engineering: A,* vol. 647, pp. 74–83, 2015.
3. B. Selvarajou, B. Kondori, A. A. Benzerga and S. P. Joshi, "On plastic flow in notched hexagonal close packed single crystals," *Journal of the Mechanics and Physics of Solids,* vol. 94, pp. 273–297, 2016.
4. M. J. Nemcko and D. S. Wilkinson, "Impact of microstructure on void growth and linkage in pure magnesium," *International Journal of Fracture,* vol. 200, no. 1–2, pp. 31–47, 2016.
5. B. Selvarajou and S. P. Joshi, "Three dimensional simulations of texture and triaxiality effects on the plasticity of magnesium alloys," *Acta Materialia,* vol. 127, pp. 54–72, 2017.
6. N. S. Prasad, R. Narasimhan and S. Suwas, "Effect of notch acuity on the fracture behavior of AZ31 Mg alloy," *Engineering Fracture Mechanics,* vol. 187, pp. 241–261, 2018.
7. B. Selvarajou and S. P. Joshi, "Void growth and coalescence in hexagonal close packed crystals," *Journal of the Mechanics and Physics of Solids,* vol. 125, pp. 198–224, 2019.
8. P. P. Indurkar and S. P. Joshi, "Void Growth and Coalescence in Porous Plastic Solids With Sigmoidal Hardening," *Journal of Applied Mechanics,* vol. 86, no. 9, 2019.
9. J. Zhang and S. P. Joshi, "Phenomenological crystal plasticity modeling and detailed micromechanical investigations of pure magnesium," *Journal of the Mechanics and Physics of Solids,* vol. 60, no. 5, pp. 945–972, 2012.
10. R. Quey, P. R. Dawson and F. Barbe, "Large-scale 3D random polycrystals for the finite element method: Generation, meshing and remeshing," *Computer Methods in Applied Mechanics and Engineering,* vol. 200, no. 17, pp. 1729–1745, 2011.
11. F. Bachmann, R. Hielscher and H. Schaeben, "Texture analysis with MTEX - free and open source software toolbox," in *Solid State Phenomena*, Trans Tech Publ, 2010, pp. 63–68.